



Anisotropic evolutions of the magnetohydrodynamic Richtmyer-Meshkov instability induced by a converging shock

Jianhua Qin 

Interdisciplinary Center for Fundamental and Frontier Sciences, Nanjing University of Science and Technology, Jiangyin 214443, China

Guodan Dong *

The State Key Laboratory of Nonlinear Mechanics, Institute of Mechanics, Chinese Academy of Sciences, Beijing 100190, China and School of Engineering Sciences, University of Chinese Academy of Sciences, Beijing 100049, China

 (Received 20 May 2023; revised 24 July 2023; accepted 2 October 2023; published 1 November 2023)

The investigation of the converging shock-induced Richtmyer-Meshkov instability, which arises from the interaction of converging shocks with the interface between materials of differing densities in cylindrical capsules, is of significant importance in the field of inertial confinement fusion (ICF). The use of converging shocks, which exhibit higher efficiency than planar shocks in the development of the RMI due to the Bell-Plesset effects, is particularly relevant to energy production in the ICF. Moreover, external magnetic fields are often utilized to mitigate the development of the RMI. This paper presents a systematic investigation of the anisotropic nature of the Richtmyer-Meshkov instability in magnetohydrodynamic induced by the interaction between converging shocks and perturbed semicylindrical density interfaces (DI) based on numerical simulations using Athena++. The results reveal that magnetic fields with $\beta = 1000$, 100, and 10 (β is defined as the ratio of the plasma pressure to the magnetic pressure) lead to an anisotropic intensification of magnetic fields, anisotropic accelerations of various shock waves [including the converging incident shock (CIS), transmitted shock (TS), and reflected shock (RS)], and anisotropic growth of the DI with subsequent anisotropic vorticity distribution. Upon closer inspection, it becomes evident that these phenomena are strongly interconnected. In particular, the region where the wave front of the CIS impacts the middle point of semicylindrical DI, where the magnetic field is more perpendicular to the fluid motion, experiences a more significant amplification of the magnetic fields. This generates higher-pressure jumps, which in turn accelerates the shock wave near this region. Furthermore, the anisotropic amplification of the magnetic fields reduces the movement of the RMI near the middle point of semicylindrical DI and leads to the anisotropic formation of RMI-induced bubbles and spikes, as well as vortices. By examining vorticity distributions, the results underscore the crucial role of magnetic tension forces in inhibiting fluid rotation.

DOI: [10.1103/PhysRevE.108.055201](https://doi.org/10.1103/PhysRevE.108.055201)

I. INTRODUCTION

Shock waves accelerating a density interface cause complex physical phenomena, including the interface amplitude growth, wave pattern evolution, and vorticity generation [1–3]. Richtmyer introduced the linear theory for this process in 1960 [4], which was later confirmed by Meshkov's shock tube experiments [5]. This impulsive version of the Rayleigh-Taylor instability (RTI) [6,7] is known as the Richtmyer-Meshkov instability (RMI) [8].

Over the past few decades, considerable efforts have been devoted to studying the RMI in hydrodynamics (Hydro-RMI) and RMI in magnetohydrodynamics (MHD-RMI) due to their importance in various engineering applications and universal occurrence. For instance, in inertial confinement fusion (ICF), the Hydro-RMI promotes mixing between shell material and fuel, leading to a reduction in the compression of the inner material, thus affecting ICF performance [9–12]. As

an alternative to ICF, magnetic confinement fusion (MCF) creates nuclear fusion reactions by confining plasma using magnetic fields [13]. To counteract the undesired effect of the Hydro-RMI in ICF, devices based on the idea of magnetized liner inertial fusion (MagLIF) are under development, which achieves high fusion yields with relatively low-cost equipment [14,15]. Hohenberger *et al.* [16] found that applying external magnetic fields increases production at the OMEGA Laser Facility of the Laboratory for Laser Energetics. In supersonic combustion systems, the Hydro-RMI accelerates the mixing of fuel and oxidizer, thereby enhancing combustion efficiency [17]. During a supernova, the interaction between inhomogeneous density materials and high Mach number flows triggers the RMI [18], and the ionized materials of supernova remnants interact with magnetic fields [19].

The orientation of the initial magnetic field is a crucial factor in the suppression of the RMI. By investigating the RMI in an oblique planar contact discontinuity using advanced numerical methods, Samtaney [20] primarily demonstrated that longitudinal magnetic fields, which are perpendicular to the incident wave front, can suppress the growth rate of the RMI.

*dongguodan@imech.ac.cn

Wheatley *et al.* [21] subsequently conducted a study to determine the detailed mechanism for the suppression of the RMI also under a longitudinal magnetic field. They noted that the magnetic field generates a series of planar waves, including the Alfvén wave, during the refraction process, which effectively transports unstable vorticities away from the density interface. As a result, the vorticity deposition on the density interface is reduced, resulting in a smoother interface. To examine the impact of longitudinal magnetic fields on the RMI, Wheatley *et al.* [22] employed the Laplace transform within the framework of ideal incompressible magnetohydrodynamics (MHD). They solved the linearized initial value problem analytically and discovered that while the magnetic field did not affect the initial growth rate of the RMI, it did suppress the growth rate at a later stage. In the subsequent work, Wheatley *et al.* [23] investigated the effects of various initial features, including the incident shock strength, magnetic field strength, and perturbation amplitude, on the RMI.

Recent analytical and numerical investigations have focused on the effect of a transverse magnetic field, which is parallel to the incident wave front [24–28]. In the framework of ideal incompressible MHD, Cao *et al.* [24] illustrated that the interface instabilities can be stabilized by the Lorentz force in the transverse magnetic field. In their study, the initial magnetic field has the same perturbations and jumps just like the velocity field. Meanwhile, Qiu *et al.* [29] investigated the effects of transverse magnetic fields and viscosity on the RMI. Their analytical study showed that the magnetic field provides oscillation and damping, while viscosity only provides damping. By considering a more general case where the initial magnetic field is uniformly distributed, Wheatley *et al.* [27] studied the effect of the transverse magnetic field on the RMI. In their simulation, magnetic field lines penetrated through perturbed density interfaces, and the results indicated that the RMI is also suppressed by this kind of magnetic field. While the RMI is influenced by the magnetic field, the magnetic field is also influenced by the RMI. Zhang *et al.* [28] demonstrated that the magnetic tension generates a torque on the interface fluid that opposes the torque caused by the velocity shear, resulting in the suppression of the Kelvin-Helmholtz instability (KHI) on the density interface. Combining two-dimensional numerical investigations with single-mode analysis, Sano *et al.* [19] demonstrated that magnetic fields can be amplified by the RMI. The saturation level of the magnetic field is determined by the relation between the thermal pressure and the magnetic pressure.

The preceding analysis of the MHD-RMI primarily centers on the instability induced by a planar shock. Measuring a planar shock in a single experiment is relatively straightforward compared to a converging shock, which intensifies as it propagates inward, necessitating the consideration of both temporal and spatial gradients. Thus, earlier investigations of the Hydro-RMI and MHD-RMI measurements have primarily concentrated on planar geometries. Nevertheless, in ICF, cylindrical material capsules are used, and the detonation and chemical reactions are triggered by converging incident shock waves. Hence, exploring the RMI triggered by converging incident shocks is more practical and promising.

The investigation of the converging shock-induced Hydro-RMI, which arises from the interaction of converging shocks

with the interface between materials of differing densities in cylindrical capsules, is of significant importance in ICF. The use of converging shocks is particularly relevant to energy production. This is because the converging configuration exhibits higher efficiency than the planar configuration in RMI development due to its higher perturbation growth rate, which is known as the Bell-Plesset effects [30–32]. Mikaelian [33] extended the linear analysis of Plesset [31] to the spherical system composing multiple concentric incompressible fluid shells and investigated the RMI and RTI of the system. Zhang and Graham [34] conducted one of the early investigations on Hydro-RMI in cylindrical geometry. Their numerical study involved examining the imploding and exploding shocks for both positive and negative Atwood numbers, which are defined as the density difference between two fluids normalized by their sum. To investigate the linear stability of RMI and RTI in concentric cylindrical shells, Mikaelian developed a theoretical model to estimate the mixing layer width between different fluids [35]. The work of Mikaelian included discussing the freeze-out phenomena, which leads to a zero asymptotic growth rate through numerical simulations and developing a simple model for the evolution of turbulent mixing. Lombardini and Pullin [36] then investigated the RMI in cylindrical and spherical geometries with azimuthal and axial perturbations and developed a linear incompressible theory for the case of an imploding or exploding shock. They developed a theory for the asymptotic growth rate of perturbations and derived a unified expression for the asymptotic impulsive growth rate in planar, cylindrical, and spherical cases. Their work was complemented and verified by compressible nonlinear simulations with small amplitude perturbations. However, the model of Lombardini and Pullin did not capture the typical scenario in converging geometry where the RMI is usually followed by the RTI due to the continued acceleration or deceleration of the interface towards the center of convergence, depending on the sign of the Atwood number. As the physical configuration that is relevant to ICF involves a converging shock, it is of great interest to examine the RMI in a converging geometry, especially in the presence of a magnetic field, and investigate any physical mechanisms of suppression. In the area of experimental investigation, apart from theoretical and numerical studies, Ding *et al.* [37] first measured the perturbation amplitude in the converging Hydro-RMI using shock tube measurements. To forecast the perturbation growth in a converging geometry from early to late stages before the reshock, they introduced a modified model based on Bell's equation with the inclusion of a decay factor.

In the context of ICF implosion, the high temperatures lead to rapid ionization of the involved materials, resulting in the interaction between the conducting fluids and imposed or self-generated magnetic fields [38,39]. Therefore, the MHD-RMI of the cylindrical density interface driven by converging shock waves has recently attracted tremendous attention [26,40–42]. Mostert *et al.* [40] explored the impact of seed magnetic fields on the RMI in cylindrical and spherical scenarios, while Bakhsh *et al.* [41] observed that compressing the RMI could be achieved by a magnetic field, given that the Alfvén wave fronts helped to transport the vorticity. The research of Mostert *et al.* [42] presented the effects of octahedrally symmetric magnetic fields on the RMI in spherical

implosions. Black *et al.* [43] studied the MHD-RMI evolution in cylinder cases by varying the magnetic orientation (longitudinal or transverse), Mach number ($Ma = 1.2, 1.66, \text{ and } 2.2$), and magnetic field strengths (100, 250, and 500 G). In the framework of Hall-magnetohydrodynamics, Shen *et al.* [44] presented the suppression of the RMI under the Hall-MHD description. In their research, they found that when the ion skin depth is finite, the vorticity dynamics responsible for the suppression of RMI exhibit significant differences from the ideal MHD-RMI flow. Most previous MHD studies solely focused on single-mode density interfaces. However, Dong *et al.* [45,46] investigated triangular and cylindrical interfaces without perturbations and demonstrated that the RMI could also be suppressed by the magnetic field in closed interfaces. Using dynamic mode decomposition, Dong *et al.* [46] showed that small vorticity structures with high frequencies were compressed by the magnetic fields. Qin and Dong [26] also revealed that the growth rate of the RMI and strength of the induced magnetic fields were determined by the curvature of the density interface.

The novelty of the present work underpins the deep and detailed understanding of the anisotropic features of the MHD-RMI induced by the converging incident shock, which to our best knowledge, has not yet been systematically studied. Due to the effect of the directional magnetic fields, the anisotropic properties of the flow appear [47]. In this work, the anisotropic amplification of the magnetic fields, the anisotropic acceleration of the converging incident shock (CIS), the reflected shock (RS), and transmitted shock (TS), as well as the anisotropic evolution of the density interfaces and the vorticities are discussed. Within this paper, we employ the term ‘‘anisotropic’’ to characterize the flow rather than ‘‘asymmetric’’. This choice is made due to the fact that fields such as density schlieren, vorticity, and magnetic fields maintain symmetry along specific directions throughout the converging shock-interface interactions in MHD. The focus of previous investigations on shock-density interface interactions in the MHD is on the suppression of the RMI caused by the restoring magnetic tension force. However, apart from the magnetic tension force, the magnetic pressure force could also exist near the density interface with the possibility to affect the flow field. The acceleration of the solar wind is commonly attributed to the Alfvén wave, as described in studies such as De Pontieu *et al.* [48] and McIntosh *et al.* [49]. In this work, we will show when and how the magnetic pressure force will also affect the evolution of the flow. Furthermore, to demonstrate that the incident wave and reflected wave speed could also be influenced by the magnetic field, especially in the transverse magnetic field, a detailed investigation has been conducted to show the anisotropic development of the wave speeds of the CIS, RS, and TS in the MHD cases.

This paper is structured as follows: We first present initial conditions and the ideal MHD equations and numerical methods in Sec. II A. Then, the computational setup and validations are shown in Sec. II B. After that, the results and discussions are presented in Sec. III, including the anisotropic amplification of the magnetic field (Sec. III A), anisotropic acceleration of shock waves (Sec. III B), and anisotropic density interface evolution and the vorticity distributions (Sec. III C). In the end, a summary of this paper is given in Sec. IV.

II. NUMERICAL METHODS AND COMPUTATIONAL SETUPS

A. Governing equations and numerical methods

MHD is a fluid description of plasmas. The ideal MHD equations, under the assumptions of compressibility, adiabaticity, and inviscid flow, are given in nondimensionalized form as

$$\frac{\partial \rho}{\partial t} + \nabla \cdot (\rho \mathbf{u}) = 0, \quad (1)$$

$$\frac{\partial \rho \mathbf{u}}{\partial t} + \nabla \cdot (\rho \mathbf{u} \mathbf{u} - \mathbf{B} \mathbf{B}) + \nabla (p + B^2/2) = \mathbf{0}, \quad (2)$$

$$\frac{\partial e}{\partial t} + \nabla \cdot [(e + p + B^2/2) \mathbf{u} - \mathbf{B}(\mathbf{B} \cdot \mathbf{u})] = 0, \quad (3)$$

$$\frac{\partial \mathbf{B}}{\partial t} - \nabla \times (\mathbf{u} \times \mathbf{B}) = \mathbf{0}, \quad (4)$$

$$e - \frac{p}{(\gamma - 1)} - \frac{\rho u^2}{2} - \frac{B^2}{2} = 0, \quad (5)$$

in which γ , ρ , \mathbf{u} , \mathbf{B} , p , and e are the ratio of specific heats, mass density, the velocity vector, the magnetic field vector, the gas pressure, and the total energy density, respectively. In addition, $u^2 = \mathbf{u} \cdot \mathbf{u}$ and $B^2 = \mathbf{B} \cdot \mathbf{B}$. Here the variables are nondimensionalized from the physical mass density of air ($\tilde{\rho}_1$ as will be given in Sec. II B), reference length scale (\tilde{L}_0), speed of sound in the air (\tilde{V}_c), and permeability of vacuum ($\tilde{\mu}_0$). Specifically, the nondimensionalized variables in Eqs. (1)–(5) are defined as $\rho = \tilde{\rho}/\tilde{\rho}_1$, $t = \tilde{t}/(\tilde{L}_0/\tilde{V}_c)$, $\nabla = \tilde{L}_0 \tilde{\nabla}$, $\mathbf{u} = \tilde{\mathbf{u}}/\tilde{V}_c$, $\mathbf{B} = \tilde{\mathbf{B}}/\sqrt{\tilde{\mu}_0 \tilde{V}_c^2 \tilde{\rho}_1}$, $p = \tilde{p}/(\tilde{V}_c^2 \tilde{\rho}_1)$, and $e = \tilde{e}/(\tilde{V}_c^2 \tilde{\rho}_1)$. In addition, the nondimensional length is defined as $L = \tilde{L}/\tilde{L}_0$. It is necessary to clarify that throughout this paper, the variables denoted with the ‘‘ \sim ’’ symbol represent physical units, while those without the symbol represent nondimensional units.

To numerically solve the aforementioned ideal MHD equations, we utilize a suite of algorithms. The second-order predictor-corrector time integrator developed by van Leer is employed for time advancement [50], while the piecewise linear method in conjunction with the van Leer limiter is utilized for nonoscillatory spatial reconstructions. The Harten-Lax-van Leer discontinuities (HLLD) approximate Riemann solver is adopted to compute upwind fluxes and electric fields at cell faces [51]. To maintain the divergence-free constraint of the magnetic field (i.e., $\nabla \cdot \mathbf{B} = 0$) due to Gauss’s law for magnetism, we employ the constrained transport algorithm. These algorithms have been validated and verified by Stone *et al.* [52] and White *et al.* [53], and have also been successfully used to investigate the RMI involving light bubbles in both hydrodynamics and MHD [46]. The simulations presented in this study are conducted using the open-source software Athena++ [52,53].

B. Computational setups and validations

The discussions in Sec. III are based on the simulations using the experimental configuration outlined in Ding *et al.* [37], with a specific emphasis on investigating the Richtmyer-Meshkov instability induced by a single perturbed cylindrical interface in a shocked medium. The interface shape is modeled after the air-SF₆ sinusoidal gaseous interface created by

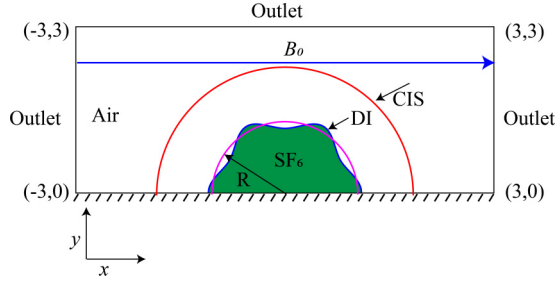


FIG. 1. Computational domain. The red line represents the initial position of the converging incident shock (CIS), the blue arrow line represents the initial magnetic field (B_0), and the blue line is the initial density interface (DI), which is the pink line superimposed with sinusoidal perturbations.

a soap film in the experimental study of Ding *et al.* The mass density of the air and SF_6 gases are $\tilde{\rho}_1 = 1.19 \text{ kg/m}^3$ and $\tilde{\rho}_2 = 5.95 \text{ kg/m}^3$ in physical units, respectively. As shown in Fig. 1, by nondimensionalizing the length with $\tilde{L}_0 = 0.025 \text{ m}$, the simulation domain for the present study is a rectangular area of $[-3, 3] \times [0, 3]$, where the cylindrical interface is centered at $(0, 0)$. The initial density interface (DI) has a radius of $R = 1$ and is perturbed with an amplitude of $a = 0.04$ using the coordinate $r = R + a \sin(n\theta + \pi/2)$, where n is the azimuthal mode number and θ is the azimuthal angle. The converging incident shock (CIS) is applied with a Mach number of $Ma = \tilde{V}_{CIS}/\tilde{V}_c = 1.33$ and it is initially a semi-circle centered at $(0,0)$ with a radius 1.544, in which \tilde{V}_{CIS} and \tilde{V}_c are the speed of the converging incident shock and the sound speed of air, respectively. The preshock pressure is set to the atmospheric pressure of $\tilde{p}_0 = 1.017 \times 10^5 \text{ Pa}$. The permeability of vacuum is $\tilde{\mu}_0 = 4\pi \times 10^{-7} \text{ N A}^{-2}$. Because the fluid for the simulations in Sec. III is considered to be plasmas, the ratio of specific heats is chosen as $\gamma = 5/3$. Therefore, $\tilde{V}_c = \sqrt{\tilde{p}_0 \gamma / \tilde{\rho}_0} = 377.4 \text{ m/s}$. The uniformly distributed magnetic field is along x direction with a magnitude of B_0 . Moreover, the left, right, and upper boundaries are modeled as outflow boundaries, while a solid wall boundary condition is applied to the bottom boundary. The remaining dimensionless parameters used for the initialization can be obtained from the nondimensionalization process introduced in Sec. II A as $V_c = 1.0$, $p_0 = 0.6$, $\rho_1 = 1.0$, and $\rho_2 = 5.0$.

A validation study of the hydrodynamic RMI induced by the interaction of the converging shock and a semicylindrical interface without perturbations ($a = 0$) is presented, in addition to our previous studies in both Hydro-RMI and MHD-RMI induced by planar incident shocks [26,45,46]. In this validation case, to compare the results with Ding *et al.* [37], $\gamma = 1.4$ and $\tilde{V}_c = 345.9 \text{ m/s}$ are used for the air at the room temperature according to Refs. [37,54]. Other parameters including the Mach number, gas densities, initial density interface radius, and position of the converging initial shock are the same as the computational setup. Comparisons of wave patterns and radius of the waves against time obtained from our numerical simulations using a mesh of 1800×900 with the experimental results are shown in Figs. 2 and 3, respectively. These two figures demonstrate good agreement between the simulated and experimental results. Compared to the experimental results, the complex wave configuration

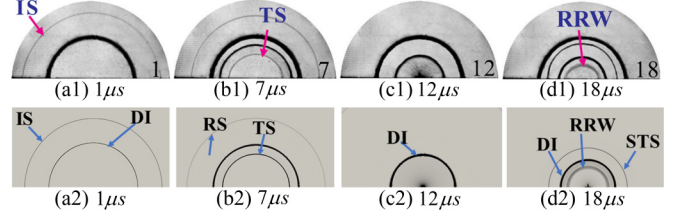


FIG. 2. Validation of our converging shock numerical results (the second row) by comparing them with the experimental results shown in Ref. [37] (the first row). IS: Incident shock; DI: Density interface; TS: Transmitted shock; RS: Reflected shock; STS: Secondary transmitted shock; RRW: Reflected rarefaction waves. The thickest black line that exists in the first row is the position of the soap film device.

is more clearly captured in our numerical simulations due to the unavoidable noise present in laboratory experiments. It is worth noting that the thickest black lines in all figures in the first row are the position of the soap film device.

To ensure accurate and efficient numerical simulations for the remainder of this study, a grid convergence analysis was conducted. Specifically, the interaction between a converging shock wave and a perturbed semicylindrical density interface was considered in a rectangular domain of $[-3, 3] \times [0, 3]$ discretized using uniform Cartesian meshes. Three sets of meshes, denoted as “coarse,” “medium,” and “fine,” corresponding to 900×450 , 1800×900 , and 2400×1200 grids, respectively, were tested. The results of this analysis are shown in Fig. 4. Specifically, the pressure jump predicted by the medium and fine meshes showed good agreement, while the results of the coarse grid were somewhat different in comparison. Based on considerations of both computational efficiency and accuracy, the medium mesh was selected for subsequent simulations.

III. RESULTS AND DISCUSSIONS

We investigate the converging incident shock-induced RMI in both hydrodynamics and MHD. For MHD cases, three

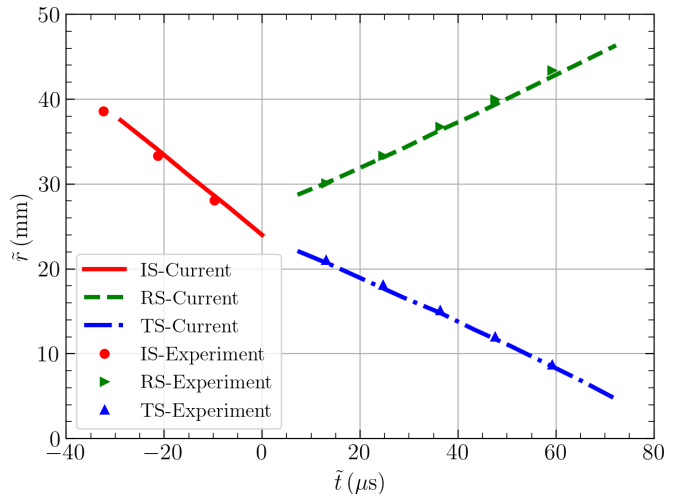


FIG. 3. Comparisons of the radius of the incident shock (IS), rarefaction shock (RS), and transmitted shock (TS) waves against time obtained by our present simulation and the experimental result of Ding *et al.* [37].

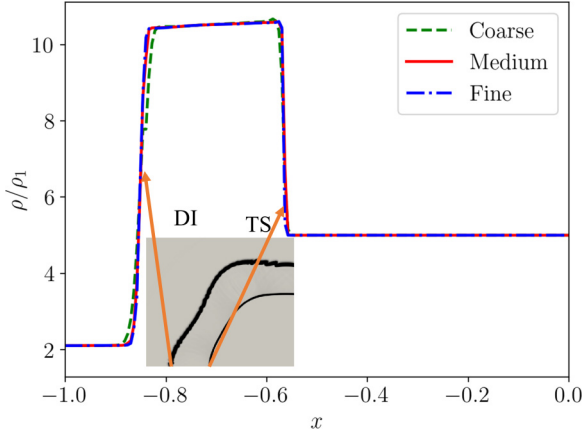


FIG. 4. Grid convergence study for the interaction between the converging incident shock and the perturbed semicircular density interface. The curves depicted in the figure are obtained from $y = 0$ at $t = 0.1$. Green dashed line: Coarse grid with 900 and 450 cells in the x and y directions, respectively. Red solid line: Medium grid with 1800 and 900 cells in the x and y directions, respectively. Blue dash-dot line: Fine grid with 2400 and 1200 cells in the x and y directions, respectively.

different magnetic fields with nondimensional strengths of $\beta = 1000, 100$, and 10 are imposed in the x direction, in which β is defined as

$$\beta = \frac{2\tilde{p}_0}{\tilde{B}_0^2/\tilde{\mu}_0} = \frac{2p_0}{B^2}. \quad (6)$$

A. Anisotropic amplification of the magnetic field

Figure 5 displays the spatial distribution of the amplified magnetic field. The amplification of the magnetic field exhibits anisotropy in which a greater enhancement is observed near point A [marked as A in Fig. 5(c)], where u_y

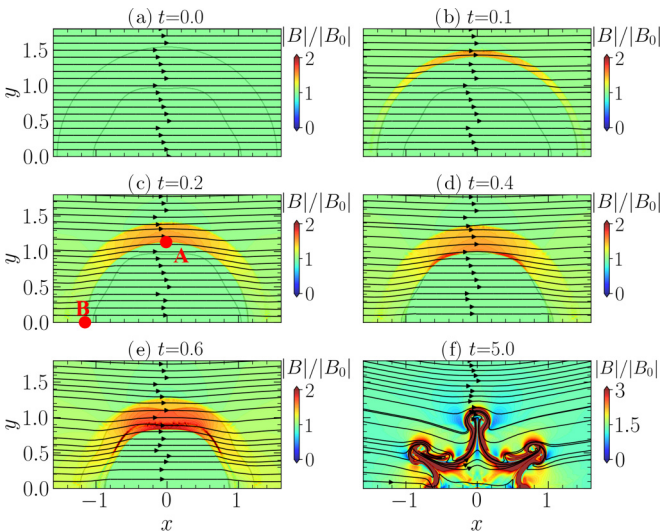


FIG. 5. Contours for the amplification of the magnetic field at different instants in the $\beta = 1000$ case. (a) $t = 0$; (b) $t = 0.1$; (c) $t = 0.2$; (d) $t = 0.4$; (e) $t = 0.6$; (f) $t = 5$. The black lines with arrows in the figure represent the magnetic field lines.

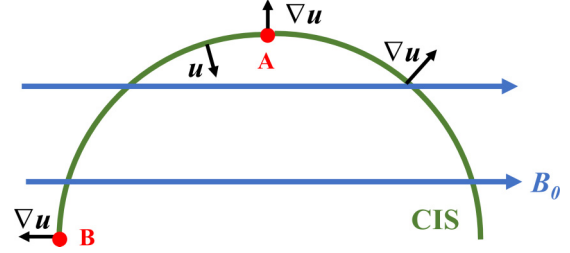


FIG. 6. Schematic of the anisotropic amplification of the magnetic fields. CIS: The incident shock wave. B_0 : The initial magnetic field. Points A and B represent the typical position where only u_y and u_x appear, respectively.

predominates and the angle between \mathbf{B} and \mathbf{u} is nearly perpendicular initially. Additionally, the magnetic field lines appear more densely concentrated in this area, yet they are noticeably more distorted near point B [marked as B in Fig. 5(c)], where u_x is dominant and \mathbf{B} and \mathbf{u} are nearly parallel.

To provide insight into the underlying mechanism of these phenomena, the magnetic induction equation is analyzed, which is presented below as

$$\begin{aligned} \frac{\partial \mathbf{B}}{\partial t} &= \nabla \times (\mathbf{u} \times \mathbf{B}) \\ &= \mathbf{u}(\nabla \cdot \mathbf{B}) - \mathbf{B}(\nabla \cdot \mathbf{u}) + (\mathbf{B} \cdot \nabla)\mathbf{u} - (\mathbf{u} \cdot \nabla)\mathbf{B}, \end{aligned} \quad (7)$$

in which the first term on the right-hand side (RHS) is zero due to the divergence-free constraint of the magnetic field ($\nabla \cdot \mathbf{B} = 0$). In Eq. (7), the compression term $[\mathbf{B}(\nabla \cdot \mathbf{u})]$ describes the change in the magnetic field due to the divergence of the fluid velocity field. However, for all cases considered in this study with $\text{Ma} = 1.33$, this term should be negligible. The third term $[(\mathbf{B} \cdot \nabla)\mathbf{u}]$ is the stretching/shearing term, which describes the stretching/shearing of the magnetic field lines due to the fluid flow in certain directions, leading to an anisotropic amplification of the magnetic field. The last term, $(\mathbf{u} \cdot \nabla)\mathbf{B}$, is called the advection term, indicating the transport of the magnetic field by the velocity field. Specifically, it describes how the fluid motion can cause the magnetic field lines to become distorted and lead to the amplification of magnetic fields in regions where there is strong advection, such as in turbulent or shock-driven flows.

Therefore, Eq. (7) can be shortened as

$$\frac{\partial \mathbf{B}}{\partial t} = (\mathbf{B} \cdot \nabla)\mathbf{u} - (\mathbf{u} \cdot \nabla)\mathbf{B}. \quad (8)$$

Initially, the last term in the RHS of Eq. (8) also disappears since the uniform magnetic field is applied. Thus, the initial evolution of the magnetic field is mainly influenced by the stretching of the magnetic field due to the motion of the fluid and can be explained using

$$\frac{\partial \mathbf{B}}{\partial t} = (\mathbf{B} \cdot \nabla)\mathbf{u}. \quad (9)$$

To demonstrate the anisotropic amplification of the magnetic field in the converging shock-induced RMI, Fig. 6 is presented. As seen, the point marked by A [the same A in Fig. 5(c)] is characterized by the existence of only u_y . Then

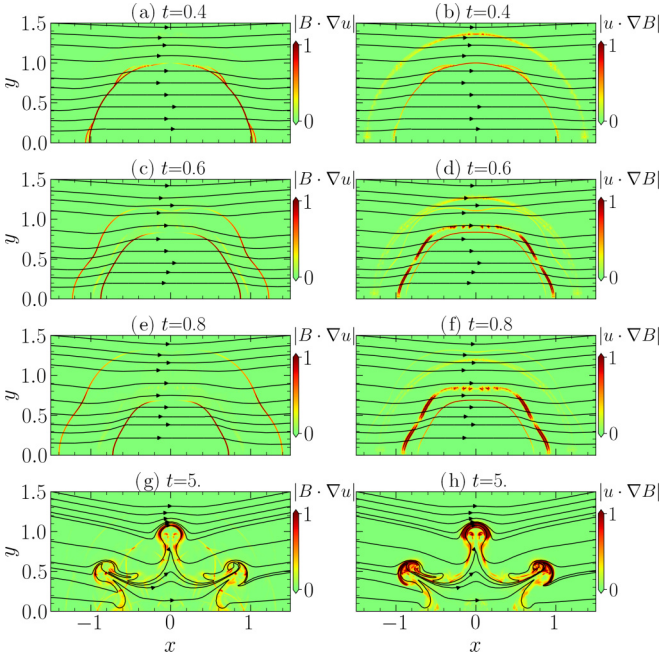


FIG. 7. Contours of the $(\mathbf{B} \cdot \nabla)\mathbf{u}$ (shown in the left column) and $(\mathbf{u} \cdot \nabla)\mathbf{B}$ (shown in the right column) terms for the amplification of the magnetic field.

$\nabla\mathbf{u}$ becomes ∇u_y , and Eq. (9) can be simplified to

$$\frac{\partial B_y}{\partial t} = (\mathbf{B} \cdot \nabla)u_y. \quad (10)$$

It can be inferred that the induction of B_y occurs in point A due to the presence of the CIS, which results in a denser distribution of magnetic field lines in this area, as depicted in Fig. 5. Conversely, in point B, the evolution of \mathbf{B} can be simplified as

$$\frac{\partial B_x}{\partial t} = (\mathbf{B} \cdot \nabla)u_x. \quad (11)$$

Therefore, the magnetic field becomes distorted in this region, which could also be identified in Fig. 5. After the initial stage, the $\nabla\mathbf{B}$ term in Eq. (8) becomes dominant. Moreover, the contour plot shown in Fig. 5 suggests that the magnetic field amplification is more significant in point A, indicating that the advection term $(\mathbf{u} \cdot \nabla)\mathbf{B}$ is the main contributor to the magnetic field amplification following the shock impact.

To further elucidate that the dominant mechanism for the amplification of the magnetic field is the advection term $(\mathbf{u} \cdot \nabla)\mathbf{B}$ after the initial stage, we compare the two terms on the RHS of Eq. (8) in Fig. 7 at four different instants ($t = 0.4, 0.6, 0.8$, and 5). The $(\mathbf{B} \cdot \nabla)\mathbf{u}$ term mainly appears on the wave front during the early stages ($t = 0.4, 0.6$, and 0.8), and becomes more prominent as more vortices form. Additionally, this term is less dominant in point A where \mathbf{B} is nearly perpendicular to $\nabla\mathbf{u}$ than in point B where \mathbf{B} is nearly parallel to $\nabla\mathbf{u}$. In combination of Fig. 5, it can be inferred that the amplification of the magnetic field after the initial stage is not primarily driven by the magnetic stretching term $(\mathbf{u} \cdot \nabla)\mathbf{B}$, as point A exhibits greater magnetic field amplification. Instead, the advection term $(\mathbf{u} \cdot \nabla)\mathbf{B}$ aligned with

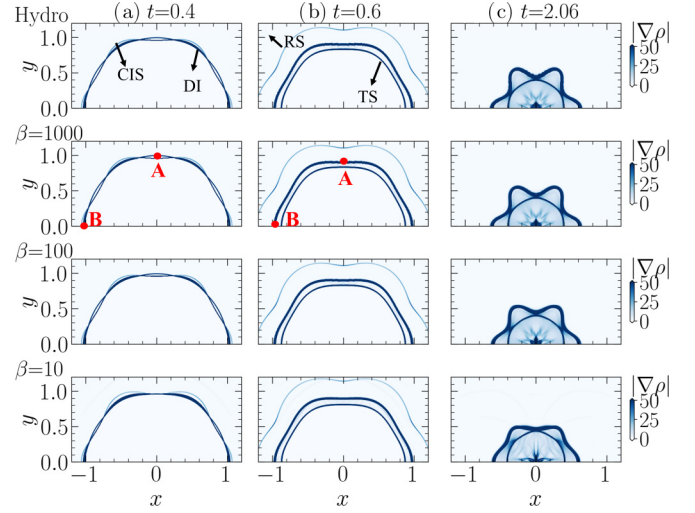


FIG. 8. Evolution of wave patterns and density interfaces in the hydrodynamic and MHD cases. (a) hydrodynamic case; (b) $\beta = 1000$; (c) $\beta = 100$; (d) $\beta = 10$. DI: Density interface; CIS: Converging incident shock wave; RS: Reflected shock wave; TS: Transmitted shock wave.

the nonuniform magnetic field is the dominant factor in the anisotropic amplification of the magnetic field, as evidenced by the amplified magnetic field in point A.

The preceding discussion reveals and analyses the anisotropic nature of the amplification of magnetic fields induced by converging shocks. Initially, the stretching term $(\mathbf{B} \cdot \nabla)\mathbf{u}$ causes the uniform magnetic field to become nonuniform, leading to a higher density of magnetic field lines in point A where the initial magnetic field is more perpendicular to the $\nabla\mathbf{u}$ and distortion in point B where the initial magnetic field is more parallel to the $\nabla\mathbf{u}$. Subsequently, the nonuniform distribution of magnetic fields is further amplified, and the anisotropy is enhanced through the influence of the advection term $(\mathbf{u} \cdot \nabla)\mathbf{B}$. Furthermore, upon further investigation, it has been found that the advection term $(\mathbf{u} \cdot \nabla)\mathbf{B}$ dominates the amplification of the magnetic field and is particularly strong in the vicinity of point A, resulting in a greater magnetic field amplification in this area.

B. Anisotropic acceleration of shock waves

In the presence of a magnetic field, shock waves also experience anisotropic accelerations, resulting in increased speeds of the CIS, TS, and RS waves as compared to the hydrodynamic scenario in specific directions. The schlieren images depicting $|\nabla\rho|$ for both the hydrodynamic and MHD cases are presented and compared in Fig. 8. As expected, following the collision of the CIS, the density interfaces (DI) become smoother with an increase in the magnetic field strength. Interestingly, the schlieren images also indicate that the wave speed can be affected by the magnetic field, particularly in the case of strong magnetic fields ($\beta = 10$). Specifically, at the instant when the CIS hits the DI at $t = 0.4$, the incident shock is observed to be accelerated in point A where it moves almost perpendicular to the magnetic field lines. Following the interaction between the CIS and DI, the reflected shock

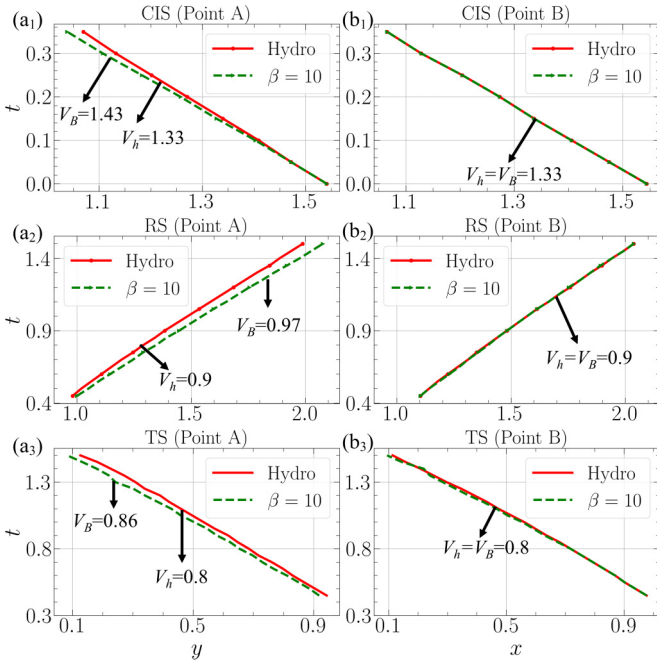


FIG. 9. Speed of the CIS, RS, and TS waves in the hydrodynamic and $\beta = 10$ cases. The left and right columns show the speed of the left and upper part for each shock as marked by A and B, respectively, as shown in Fig. 8. V_h and V_B are the corresponding wave speeds of each wave in the hydrodynamics and $\beta = 10$ cases, respectively.

wave (RS) and the transmitted shock wave (TS) are generated and travel outwards and inwards, respectively. Interestingly, a comparison of the wave patterns in the hydrodynamic and $\beta = 10$ cases at $t = 0.6$ reveals that the RS and TS are also partly accelerated by the magnetic field, as evidenced by their acceleration near point A where the magnetic field is stronger.

For a clearer comprehension of the acceleration of shock waves under the influence of a magnetic field, Fig. 9 illustrates the wave velocities of the CIS, TS, and RS marked as V_h and V_B for the hydrodynamic and $\beta = 10$ scenarios, respectively. The left and right columns of this figure illustrate the wave speeds in point A (marked as A as shown in Fig. 8) and point B (marked as B as shown in Fig. 8), respectively. Notably, the magnetic field has no effect on the speeds of each wave in point B, but speeds of the CIS, RS, and TS near point A are accelerated by the strong magnetic field. Additionally, the CIS is not accelerated during the initial stage ($t \in [0, 0.1]$), but it gains acceleration as it approaches the DI. At $t = 0.38$, the CIS hits the density interface and generates a pair of RS and TS. Specifically, the speed of the CIS in hydrodynamics is 1.33, which is consistent with our initial set of $Ma = 1.33$. However, in point A, the magnetic field accelerates it by approximately 7.5% with $V_B = 1.43$ for the $\beta = 10$ case. Similarly, the RS and TS in point A also experience an acceleration of approximately 7.5%.

In the subsequent section, the pressure distributions are analyzed to clarify the mechanism responsible for the acceleration of the shock waves. Pressure contours and magnetic field line distributions during the initial stage ($t = 0$), immediately before the CIS collides with the DI ($t = 0.2$), and

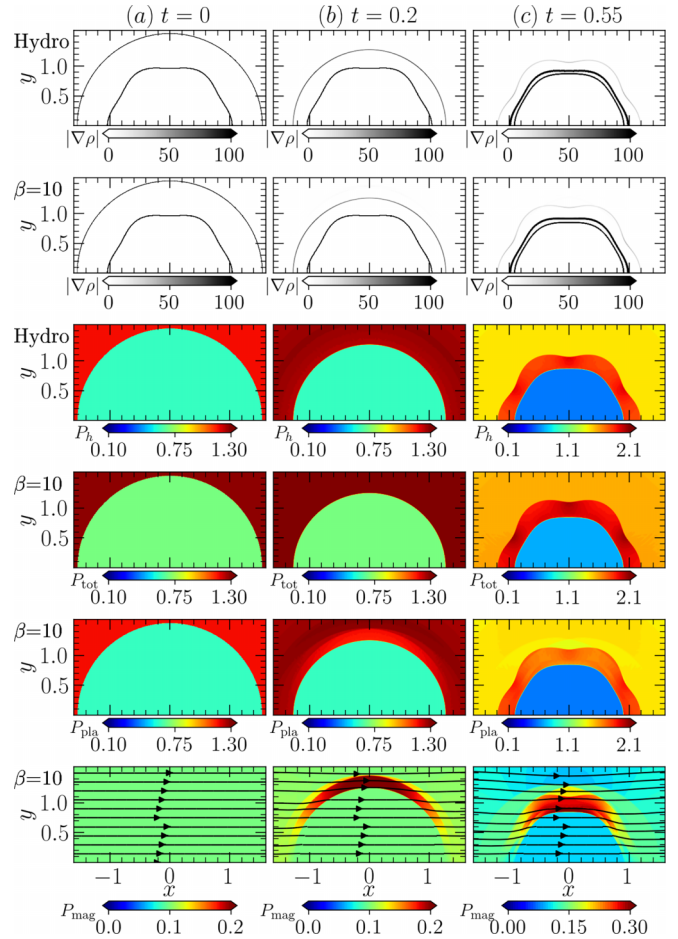


FIG. 10. The wave structures, interface structures, the distributions of pressures terms, and the magnetic field lines at the initial stage ($t = 0$), immediately before the CIS impacts the DI ($t = 0.2$), and immediately after the CIS impacts the DI ($t = 0.55$).

immediately after the CIS collides with the DI ($t = 0.55$), respectively, are illustrated in Fig. 10. The distribution of various pressure terms along line from $y = 0$ to $y = 3.0$ with $x = 0$ are plot in Fig. 11. The definition of the plasma pressure (P_{pla}) and the magnetic pressure (P_{mag}) in the MHD cases are

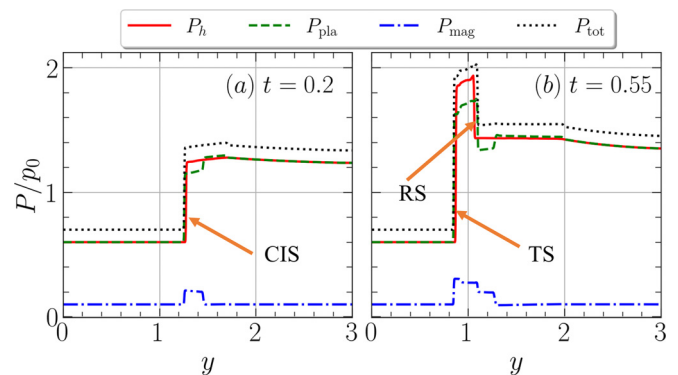


FIG. 11. Comparison of various pressures (P_h , P_{pla} , P_{mag} , and P_{tot}) distributions at $t = 0.2$ and $t = 0.55$ from $y = 0$ to $y = 3$ with $x = 0$ for the $\beta = 10$ case.

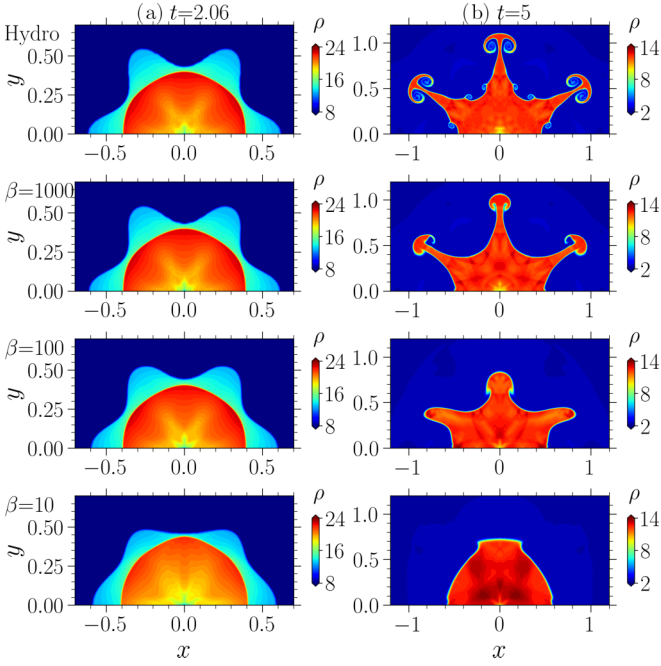


FIG. 12. Contours of the density in all cases at $t = 2.06$ (the left column) and $t = 5$ (the right column).

given as

$$\begin{aligned} P_{\text{pla}} &= p, \\ P_{\text{mag}} &= \frac{B^2}{2}, \\ P_{\text{tot}} &= P_{\text{pla}} + P_{\text{mag}}. \end{aligned} \quad (12)$$

When comparing results of $t = 0$ and $t = 0.2$ before the CIS hits the DIs, it is observed that although the initial distribution of plasma pressure P_{pla} is uniform, it becomes nonuniform and increases near the CIS in point A due to the distortion of magnetic lines in this region, which is unlike the planar shock-induced cases. Additionally, it is interesting to note that the P_{pla} carried by the fluids decreases in the region where magnetic pressure increases, leading to an increase in the magnetic field strength in this region. However, the total pressure increases near this region when compared to the corresponding hydrodynamic cases. As a result, the pressure jump before and after the shock increases, which accelerates the speed of the CIS in this region. As shown in Fig. 11(a), the magnitude of P_h are 0.6 and 1.24 before and after the CIS, respectively, while the magnitude of P_{tot} are 0.7 and 1.38 before and after the CIS, respectively. Similarly, the P_{pla} also increases near the TS and RS in point A, and the pressure jump before and after these shocks also increases as shown in Fig. 11(b). These contours reveal that the CIS, RS, and TS shocks are partly enhanced near the position where the wave front aligns more with the magnetic field lines, i.e., where the flow is more perpendicular to the magnetic field.

C. Anisotropic evolution of the RMI

In this section, we aim to examine the anisotropic progression of the MHD-RMI, with a particular emphasis on the

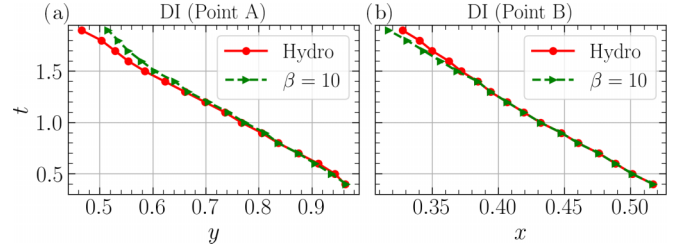


FIG. 13. Trajectories of (a) the point A (marked as A shown in Fig. 8) and (b) the point B (marked as B shown in Fig. 8) of the density interfaces in the hydrodynamics and $\beta = 10$ cases.

anisotropy development of the DI and the associated vorticity distributions. The comparison of the evolution of DIs in hydrodynamics and three MHD cases ($\beta = 1000$, 100, and 10) at two different time instances is presented in Fig. 12. Interestingly, even at $t = 2.06$, differences in the interface shape exist between the hydrodynamic and $\beta = 10$ cases. When the time reaches $t = 5$, significant differences in the interface structures can be seen for varying magnetic strengths. Additionally, in the hydrodynamic cases, the interface structure induced by the RMI, i.e., the spikes and bubbles, exhibit the same behavior near points A and B. However, even with a uniform initial magnetic field, the introduction of magnetic fields results in the formation of anisotropic spikes and bubbles.

Furthermore, the velocities of the DI at points A and B (corresponding to marked points A and B as shown in Fig. 8, respectively), where the initial magnetic field is almost parallel and perpendicular to the wave front, respectively, are compared and plotted in the left and right columns of Fig. 13. From the figure, the velocity of the DI in point A is decreased while the velocity of the DI in point B is increased. These findings collectively demonstrate the anisotropic nature of the MHD-RMI induced by converging shocks.

The subsequent discussion will examine the vorticity distributions during the early stage when the CIS impacts the DI and the later stage when dominant waves (e.g., CIS, TS, and RS *et al.*) have traversed beyond the computational domain. Figure 14 presents a comparison of the vorticity distributions in the hydrodynamic (left column) and $\beta = 10$ cases (right column) with zoomed-in details of the P1 and P2 regions in the third and fourth rows, respectively. At the instance of $t = 0.4$, the CIS impacts the DIs in the P1 region and generates the TS and RS, while the CIS has not yet reached the DIs in the P2 region. The vorticity distributions in the hydrodynamic case show that vorticities are generated upon impact and deposited on the DI, whereas in the $\beta = 10$ cases, the initial vorticities deposit on the DI but subsequently split into vorticity sheets that travel along two sides of the DIs. Furthermore, a comparison of Figs. 14(a3) and 14(b3) reveals that the distortion of the magnetic field lines leads to differences in the vorticity distributions between the hydrodynamic and $\beta = 10$ cases. Moreover, the comparison of Figs. 14(a4) and 14(b4) also shows that, in the hydrodynamic case, vorticities along the two sides of the CIS are of equal magnitude but opposite direction, while in the $\beta = 10$ case, vorticities along the two sides of the CIS are in the same direction but have different magnitudes.

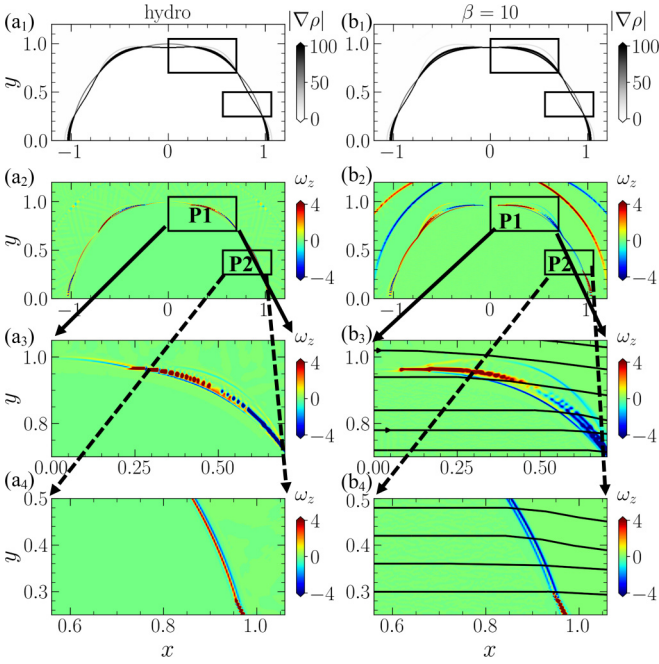


FIG. 14. Vorticity contours for the hydrodynamic (the left column) and $\beta = 10$ (the right column) cases at $t = 0.4$ with the zoomed-in details shown in the last two rows. The black solid lines in (b3) and (b4) represent the magnetic field lines. The first row is the density schlierens showing the wave and interface position.

These findings suggest that the vorticity distributions in the converging MHD-RMI are also anisotropic.

The above discussion has revealed that prior to the onset of the MHD-RMI, the vorticity distribution exhibits a degree of anisotropy. To further elucidate the mechanism responsible for the anisotropic distribution of vorticity fields observed in the MHD cases, as represented by Eq. (13), the Lorentz force is decomposed into its constituent magnetic pressure force $[\nabla(B^2/2)]$ and magnetic tension force $[(\mathbf{B} \cdot \nabla)\mathbf{B}]$:

$$f_L = (\nabla \times \mathbf{B}) \times \mathbf{B} = (\mathbf{B} \cdot \nabla)\mathbf{B} - \nabla(B^2/2). \quad (13)$$

The vector fields of the magnetic tension force and the magnetic pressure force are depicted in the second and third rows of Fig. 15, respectively. The magnitudes of these forces are higher near the wave front than near the DI. Furthermore, the magnetic pressure force is oriented in the same direction as ∇p , thereby resulting in the same direction of the vorticity according to Eq. (14). Consequently, the opposite sign of the vorticity distribution along the two sides of the shock fronts arises mainly because of the magnetic tension force, which imparts torque to the fluids.

The vorticity equation in the MHD cases is given as

$$\frac{D\boldsymbol{\omega}}{Dt} = (\boldsymbol{\omega} \cdot \nabla)\mathbf{u} - \boldsymbol{\omega}(\nabla \cdot \mathbf{u}) + \frac{\nabla \rho \times \nabla p}{\rho^2} + \nabla \times \frac{(\mathbf{B} \cdot \nabla)\mathbf{B}}{\rho} + \frac{\nabla \rho \times \nabla(B^2/2)}{\rho^2}, \quad (14)$$

where, on the right-hand side, the first term becomes negligible in two-dimensional simulations, as the vorticity vector $\boldsymbol{\omega}$ is always perpendicular to the velocity gradient vector $\nabla \mathbf{u}$. The second term, which mainly appears around the wave front

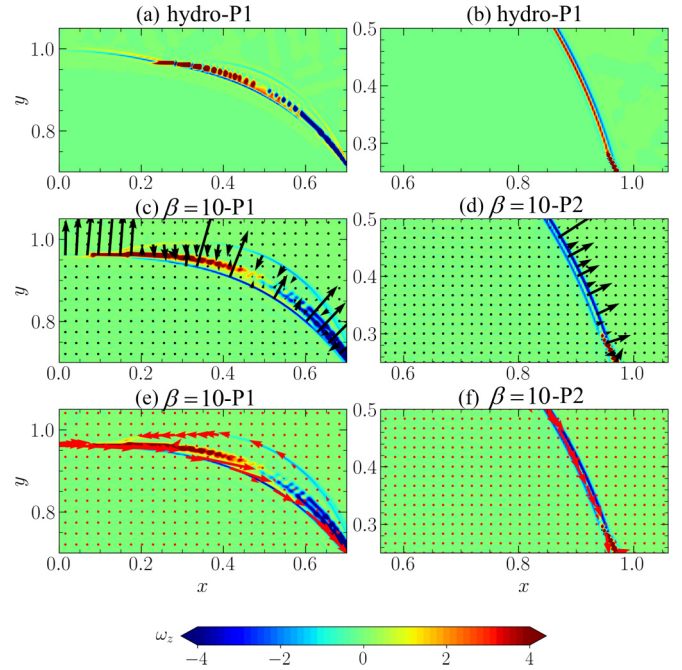


FIG. 15. Vorticity fields in the box region P1 and P2 (shown in Fig. 14) at $t = 5$ for the (a) hydrodynamic and (b, c) $\beta = 10$ cases. The black and red arrows represent the magnetic pressure force $[\nabla(B^2/2)]$ and the magnetic tension force term $[(\mathbf{B} \cdot \nabla)\mathbf{B}]$, respectively.

in the early stage, is relatively small at $Ma = 1.33$. The third term, known as the baroclinic term, is the primary cause of the RMI in hydrodynamics [26]. The fourth term is attributed to the magnetic tension forces, as shown in Eq. (13). Finally, the fifth term $\frac{\nabla \rho \times \nabla(B^2/2)}{\rho^2}$ is similar to the hydrodynamic baroclinic term $\frac{\nabla \rho \times \nabla p}{\rho^2}$.

Figure 16 depicts the vorticity distributions during the later stage of the simulation when dominant waves (e.g., CIS, TS, and RS *et al.*) have almost traveled outside the computational domain and the RMI-induced bubbles and spikes have become evident. From Fig. 16(f), the vorticity distribution is anisotropic and variations can be identified between the hydrodynamic and $\beta = 1000$ cases. The vector fields of the ∇P_{tot} are presented in Figs. 16(d) and 16(f), denoted by black arrows. Notably, the ∇P_{tot} is almost aligned with the corresponding ∇p displayed in the hydrodynamic cases, albeit with different magnitudes.

Then, Fig. 17 provides a detailed comparison of all terms involved in inducing the development of vorticity. In both the hydrodynamic and MHD cases, the ∇p term exhibits almost the same direction and amplitude. However, the $\nabla(B^2/2)$ term tends to be in the opposite direction to ∇p , thereby reducing the effect of the baroclinic effects. However, the magnetic tension term dominates over the other two forces, and it is asymmetric along the two sides of the vortices. In the context of MHD cases, the magnetic tension force functions as a torque that hinders the rotation of fluids surrounding the RMI bubbles and spikes. Consequently, the final DI and vortices exhibit anisotropy.

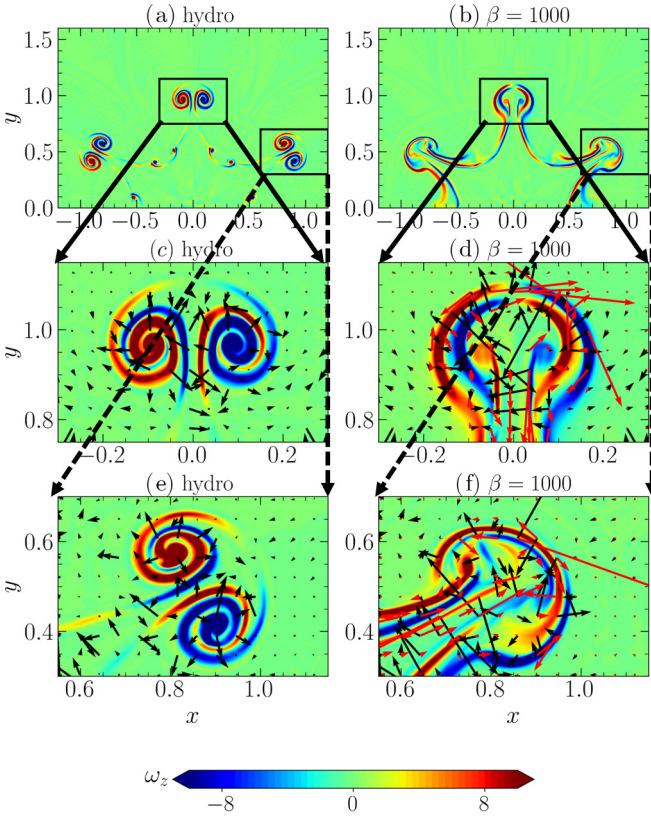


FIG. 16. Vorticity contours for the hydrodynamic (the left column) and $\beta = 1000$ (the right column) cases at $t = 5$ with the zoomed-in details shown in the last two rows. In panels (c) and (d) the black arrows represent the ∇p ; in panels (d) and (f) the black and red arrows are ∇p_{total} and $(\mathbf{B} \cdot \nabla)\mathbf{B}$, respectively.

IV. CONCLUSIONS

In summary, this study investigates the effect of magnetic fields on the converging shock-induced Richtmyer-Meshkov instability (RMI) using numerical simulations. The investigation involves the interaction between a converging shock wave and a semicylindrical density interface (DI) under both hydrodynamic and magnetohydrodynamic (MHD) conditions, considering three different magnetic field strengths. Initially, the magnetic field is uniformly distributed. The findings presented in this study offer significant insights into the anisotropic amplification of magnetic fields, as well as the anisotropic acceleration of shock waves, and related characteristics of the DI and vorticity distributions. To the best of our knowledge, these observations have not been discussed previously.

To demonstrate the amplification of magnetic fields in response to the application of a converging incident shock (CIS), the magnetic induction equation is analyzed. It is shown that the magnification of the magnetic field is brought about by the stretching of the magnetic field due to the fluid motion $[(\mathbf{B} \cdot \nabla)\mathbf{u}]$. The fluid motion produces varying magnitudes of magnetic field amplification along the DI, depending on the direction of the DI being examined. For example, solely B_x undergoes magnification by $\partial B_x / \partial t = (\mathbf{B} \cdot \nabla)u_x$, limited to the endpoints of the semicylindrical DI, with B_y being

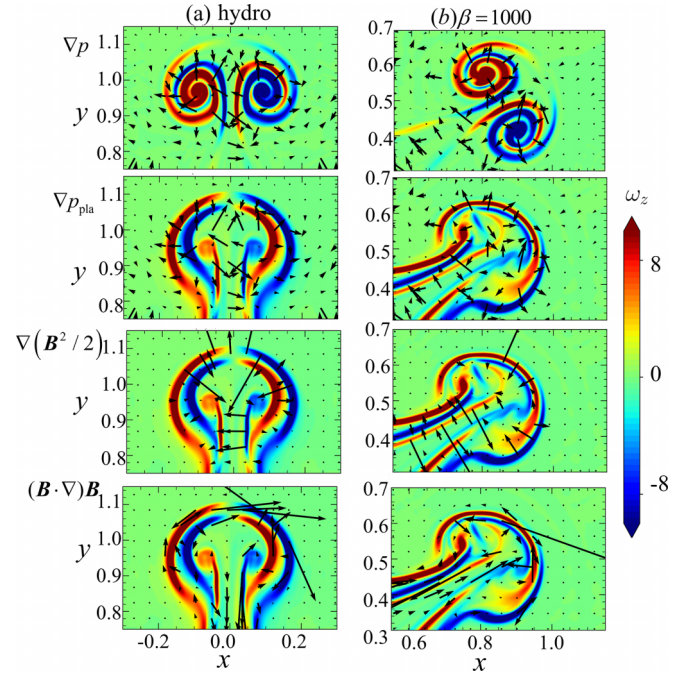


FIG. 17. Vector fields for each component of the vorticity equation (represented by black arrows) along with the contours of the vorticity field. First row: The gradient of the hydrodynamic pressure in the hydrodynamic cases; second row: The gradient of the plasma pressure the $\beta = 1000$ case; third row: The gradient of the MHD pressure the $\beta = 1000$ case; fourth row: Magnetic tension forces in the $\beta = 1000$ case.

amplified by $\partial B_y / \partial t = (\mathbf{B} \cdot \nabla)u_y$, localized to only the middle point of the DI, thus giving rise to the anisotropic magnification of the magnetic field. Additionally, the $(\mathbf{u} \cdot \nabla)\mathbf{B}$ term in the magnetic induction equation becomes apparent after the amplification of B due to the $(\mathbf{B} \cdot \nabla)\mathbf{u}$ term. Eventually, the $(\mathbf{u} \cdot \nabla)\mathbf{B}$ term dominates the anisotropic magnification of the magnetic field near the middle point of the semicylindrical DI.

Moreover, this investigation has also revealed that the CIS, the transmitted shock wave (TS), and the reflected shock wave (RS) experience partial acceleration near the middle point of the semicylindrical DI where the initial magnetic field is more perpendicular to the fluids and greater magnetic field amplification is observed. To elucidate the underlying mechanism, we compare the magnetic pressure, plasma pressure, and total pressure with the corresponding hydrodynamic pressure values immediately before, at the instant of, and immediately after the CIS impacts on the DI. The findings indicate that near the middle point of the semicylindrical DI, the total pressure (the sum of magnetic and plasma pressure) is higher than the hydrodynamic pressure, demonstrating the role of magnetic pressure in the acceleration of shock waves.

The exploration of the development of the semicylindrical DI has unveiled its anisotropic behavior in MHD conditions, in contrast to what is typically found in hydrodynamic conditions. Specifically, the bubble and spike structures for the RMI in hydrodynamics become asymmetric in the MHD conditions, with a stronger magnetic field resulting in a

smoother interface and eventually no observable bubble and spike structures at $\beta = 10$. Furthermore, the middle point of the semicylindrical DI experiences acceleration, while the endpoints of the semicylindrical DI undergo deceleration. At a later stage, when dominant shock waves including CIS, TS, and RS have propagated beyond the computational domain, the vorticity distributions in the MHD cases show a certain degree of anisotropy due to the influence of magnetic tension forces.

Future work could address the quantification of these anisotropies discussed in this study. Statistical measures such as variance, standard deviation, or coefficient of variation could be used to quantify the variability or dispersion of data along different directions. These measures

could provide insights into the anisotropy of the data distribution.

ACKNOWLEDGMENTS

The authors are supported by the National Natural Science Foundation of China (Grants No. 12202456 and No. 12072162), Fundamental Research Funds for the Central Universities (Grant No. AE89991/383), and China Postdoctoral Science Foundation (Grant No. 2021M693241). The authors also express their gratitude to the reviewers for their constructive and valuable comments, which have significantly improved the quality and clarity of this manuscript.

J. Qin and G. Dong contributed equally to this work.

-
- [1] M. Brouillette, The Richtmyer-Meshkov instability, *Annu. Rev. Fluid Mech.* **34**, 445 (2002).
 - [2] Q. Zhang, S. Deng, and W. Guo, Quantitative theory for the growth rate and amplitude of the compressible Richtmyer-Meshkov instability at all density ratios, *Phys. Rev. Lett.* **121**, 174502 (2018).
 - [3] Y. Liang, L. Liu, Z. Zhai, J. Ding, T. Si, and X. Luo, Richtmyer-Meshkov instability on two-dimensional multi-mode interfaces, *J. Fluid Mech.* **928**, A37 (2021).
 - [4] R. D. Richtmyer, Taylor instability in shock acceleration of compressible fluids, *Commun. Pure Appl. Math.* **13**, 297 (1960).
 - [5] E. Meshkov, Instability of the interface of two gases accelerated by a shock wave, *Fluid Dyn.* **4**, 101 (1972).
 - [6] R. Rayleigh, Investigation of the character of the equilibrium of an incompressible heavy fluid of variable density, *Proc. London Math. Soc.* **s1-14**, 170 (1882).
 - [7] G. I. Taylor, The instability of liquid surfaces when accelerated in a direction perpendicular to their planes I, *Proc. R. Soc. London A* **201**, 192 (1950).
 - [8] Y. Zhou, R. J. Williams, P. Ramaprabhu, M. Groom, B. Thornber, A. Hillier, W. Mostert, B. Rollin, S. Balachandar, P. D. Powell *et al.*, Rayleigh-Taylor and Richtmyer-Meshkov instabilities: A journey through scales, *Physica D* **423**, 132838 (2021).
 - [9] J. D. Lindl, R. L. McCrory, and E. M. Campbell, Progress toward ignition and burn propagation in inertial confinement fusion, *Phys. Today* **45** (9), 32 (1992).
 - [10] J. D. Lindl, P. Amendt, R. L. Berger, S. G. Glendinning, S. H. Glenzer, S. W. Haan, R. L. Kauffman, O. L. Landen, and L. J. Suter, The physics basis for ignition using indirect-drive targets on the National Ignition Facility, *Phys. Plasmas* **11**, 339 (2004).
 - [11] Y. Aglitskiy, A. Velikovich, M. Karasik, N. Metzler, S. Zalesak, A. Schmitt, L. Phillips, J. Gardner, V. Serlin, J. Weaver *et al.*, Basic hydrodynamics of Richtmyer-Meshkov-type growth and oscillations in the inertial confinement fusion-relevant conditions, *Philos. Trans. R. Soc. A* **368**, 1739 (2010).
 - [12] V. Smalyuk, C. Weber, O. Landen, S. Ali, B. Bachmann, P. Celliers, E. Dewald, A. Fernandez, B. Hammel, G. Hall *et al.*, Review of hydrodynamic instability experiments in inertially confined fusion implosions on national ignition facility, *Plasma Phys. Controlled Fusion* **62**, 014007 (2020).
 - [13] J. Degraeve, F. Felici, J. Buchli, M. Neunert, B. Tracey, F. Carpanese, T. Ewalds, R. Hafner, A. Abdolmaleki, D. de Las Casas *et al.*, Magnetic control of Tokamak plasmas through deep reinforcement learning, *Nature (London)* **602**, 414 (2022).
 - [14] S. A. Slutz and R. A. Vesey, High-gain magnetized inertial fusion, *Phys. Rev. Lett.* **108**, 025003 (2012).
 - [15] M. R. Gomez, S. A. Slutz, A. B. Sefkow, D. B. Sinars, K. D. Hahn, S. B. Hansen, E. C. Harding, P. F. Knapp, P. F. Schmit, C. A. Jennings *et al.*, Experimental demonstration of fusion-relevant conditions in magnetized liner inertial fusion, *Phys. Rev. Lett.* **113**, 155003 (2014).
 - [16] M. Hohenberger, P.-Y. Chang, G. Fiksel, J. Knauer, R. Betti, F. Marshall, D. Meyerhofer, F. Séguin, and R. Petrasso, Inertial confinement fusion implosions with imposed magnetic field compression using the OMEGA Laser, *Phys. Plasmas* **19**, 056306 (2012).
 - [17] J. Yang, T. Kubota, and E. E. Zukoski, Applications of shock-induced mixing to supersonic combustion, *AIAA J.* **31**, 854 (1993).
 - [18] D. Arnett, The role of mixing in astrophysics, *Astrophys. J. Suppl. Ser.* **127**, 213 (2000).
 - [19] T. Sano, K. Nishihara, C. Matsuoka, and T. Inoue, Magnetic field amplification associated with the Richtmyer-Meshkov instability, *Astrophys. J.* **758**, 126 (2012).
 - [20] R. Samtaney, Suppression of the Richtmyer-Meshkov instability in the presence of a magnetic field, *Phys. Fluids* **15**, L53 (2003).
 - [21] V. Wheatley, D. Pullin, and R. Samtaney, Regular shock refraction at an oblique planar density interface in magnetohydrodynamics, *J. Fluid Mech.* **522**, 179 (2005).
 - [22] V. Wheatley, D. I. Pullin, and R. Samtaney, Stability of an impulsively accelerated density interface in magnetohydrodynamics, *Phys. Rev. Lett.* **95**, 125002 (2005).
 - [23] V. Wheatley, R. Samtaney, and D. Pullin, The Richtmyer-Meshkov instability in magnetohydrodynamics, *Phys. Fluids* **21**, 082102 (2009).
 - [24] J. Cao, Z. Wu, H. Ren, and D. Li, Effects of shear flow and transverse magnetic field on Richtmyer-Meshkov instability, *Phys. Plasmas* **15**, 042102 (2008).
 - [25] Y. Levy, S. Jaouen, and B. Canaud, Numerical investigation of magnetic Richtmyer-Meshkov instability, *Laser Part. Beams* **30**, 415 (2012).

- [26] J. Qin and G. Dong, The Richtmyer–Meshkov instability of concave circular arc density interfaces in hydrodynamics and magnetohydrodynamics, *Phys. Fluids* **33**, 034122 (2021).
- [27] V. Wheatley, R. Samtaney, D. Pullin, and R. Gehre, The transverse field Richtmyer–Meshkov instability in magnetohydrodynamics, *Phys. Fluids* **26**, 016102 (2014).
- [28] H.-H. Zhang, C. Zheng, N. Aubry, W.-T. Wu, and Z.-H. Chen, Numerical analysis of Richtmyer–Meshkov instability of circular density interface in presence of transverse magnetic field, *Phys. Fluids* **32**, 116104 (2020).
- [29] Z. Qiu, Z. Wu, J. Cao, and D. Li, Effects of transverse magnetic field and viscosity on the Richtmyer–Meshkov instability, *Phys. Plasmas* **15**, 042305 (2008).
- [30] G. I. Bell, Taylor instability on cylinders and spheres in the small amplitude approximation, Technical Report LA-1321 (Los Alamos National Laboratory, Los Alamos, 1951).
- [31] M. Plesset, On the stability of fluid flows with spherical symmetry, *J. Appl. Phys.* **25**, 96 (1954).
- [32] R. Epstein, On the Bell–Plesset effects: The effects of uniform compression and geometrical convergence on the classical Rayleigh–Taylor instability, *Phys. Plasmas* **11**, 5114 (2004).
- [33] K. O. Mikaelian, Rayleigh–Taylor and Richtmyer–Meshkov instabilities and mixing in stratified spherical shells, *Phys. Rev. A* **42**, 3400 (1990).
- [34] Q. Zhang and M. J. Graham, A numerical study of Richtmyer–Meshkov instability driven by cylindrical shocks, *Phys. Fluids* **10**, 974 (1998).
- [35] K. O. Mikaelian, Rayleigh–Taylor and Richtmyer–Meshkov instabilities and mixing in stratified cylindrical shells, *Phys. Fluids* **17**, 094105 (2005).
- [36] M. Lombardini and D. Pullin, Small-amplitude perturbations in the three-dimensional cylindrical Richtmyer–Meshkov instability, *Phys. Fluids* **21**, 114103 (2009).
- [37] J. Ding, T. Si, J. Yang, X. Lu, Z. Zhai, and X. Luo, Measurement of a Richtmyer–Meshkov instability at an Air–SF₆ interface in a semiannular shock tube, *Phys. Rev. Lett.* **119**, 014501 (2017).
- [38] M. J.-E. Manuel, C. K. Li, F. H. Séguin, J. Frenje, D. T. Casey, R. D. Petrasso, S. X. Hu, R. Betti, J. D. Hager, D. D. Meyerhofer, and V. A. Smalyuk, First measurements of Rayleigh–Taylor–induced magnetic fields in laser-produced plasmas, *Phys. Rev. Lett.* **108**, 255006 (2012).
- [39] F. Séguin, C. Li, M.-E. Manuel, H. Rinderknecht, N. Sinenian, J. Frenje, J. Rygg, D. Hicks, R. Petrasso, J. Delettrez *et al.*, Time evolution of filamentation and self-generated fields in the coronae of directly driven inertial-confinement fusion capsules, *Phys. Plasmas* **19**, 012701 (2012).
- [40] W. Mostert, V. Wheatley, R. Samtaney, and D. Pullin, Effects of magnetic fields on magnetohydrodynamic cylindrical and spherical Richtmyer–Meshkov instability, *Phys. Fluids* **27**, 104102 (2015).
- [41] A. Bakhsh and R. Samtaney, Incompressible models of magnetohydrodynamic Richtmyer–Meshkov instability in cylindrical geometry, *Phys. Rev. Fluids* **4**, 063906 (2019).
- [42] W. Mostert, D. I. Pullin, V. Wheatley, and R. Samtaney, Magnetohydrodynamic implosion symmetry and suppression of Richtmyer–Meshkov instability in an octahedrally symmetric field, *Phys. Rev. Fluids* **2**, 013701 (2017).
- [43] W. J. Black, R. C. Allen, W. C. Maxon, N. Denissen, and J. A. McFarland, Magnetohydrodynamic effects in a shock-accelerated gas cylinder, *Phys. Rev. Fluids* **4**, 043901 (2019).
- [44] N. Shen, D. I. Pullin, V. Wheatley, and R. Samtaney, Impulse-driven Richtmyer–Meshkov instability in Hall-magnetohydrodynamics, *Phys. Rev. Fluids* **4**, 103902 (2019).
- [45] G.-D. Dong, H.-H. Zhang, Z.-Y. Lin, J.-H. Qin, Z.-H. Chen, Z.-Q. Guo, and S. Sha, Numerical investigations of interactions between shock waves and triangular cylinders in magnetic field, *Acta Phys. Sin.* **67**, 204701 (2018).
- [46] G.-D. Dong, Z.-Q. Guo, J.-H. Qin, H.-H. Zhang, X.-H. Jiang, Z.-H. Chen, and S. Sha, Numerical investigations of Richtmyer–Meshkov instability in different magnetic field configurations and the corresponding dynamic mode decomposition, *Acta Phys. Sin.* **68**, 165201 (2019).
- [47] J. Marston and S. Tobias, Recent developments in theories of inhomogeneous and anisotropic turbulence, *Annu. Rev. Fluid Mech.* **55**, 351 (2023).
- [48] B. De Pontieu, S. McIntosh, M. Carlsson, V. Hansteen, T. Tarbell, C. Schrijver, A. Title, R. Shine, S. Tsuneta, Y. Katsukawa *et al.*, Chromospheric Alfvénic waves strong enough to power the solar wind, *Science* **318**, 1574 (2007).
- [49] S. W. McIntosh, B. De Pontieu, M. Carlsson, V. Hansteen, P. Boerner, and M. Goossens, Alfvénic waves with sufficient energy to power the quiet solar corona and fast solar wind, *Nature (London)* **475**, 477 (2011).
- [50] B. van Leer, Towards the ultimate conservative difference scheme. II. Monotonicity and conservation combined in a second-order scheme, *J. Comput. Phys.* **14**, 361 (1974).
- [51] T. Miyoshi and K. Kusano, A multi-state HLL approximate Riemann solver for ideal magnetohydrodynamics, *J. Comput. Phys.* **208**, 315 (2005).
- [52] J. M. Stone, K. Tomida, C. J. White, and K. G. Felker, The athena++ adaptive mesh refinement framework: Design and magnetohydrodynamic solvers, *Astrophys. J. Suppl. Series* **249**, 4 (2020).
- [53] C. J. White, J. M. Stone, and C. F. Gammie, An extension of the Athena++ code framework for GRMHD based on advanced Riemann solvers and staggered-mesh constrained transport, *Astrophys. J. Suppl. Series* **225**, 22 (2016).
- [54] T. Si, T. Long, Z. Zhai, and X. Luo, Experimental investigation of cylindrical converging shock waves interacting with a polygonal heavy gas cylinder, *J. Fluid Mech.* **784**, 225 (2015).